



## Multimode optomechanics with a two-dimensional optomechanical crystal

Madiot, Guilhem; Albrechtsen, Marcus; Stobbe, Søren; Sotomayor-Torres, Clivia M.; Arregui, Guillermo

*Published in:*  
APL Photonics

*Link to article, DOI:*  
[10.1063/5.0170883](https://doi.org/10.1063/5.0170883)

*Publication date:*  
2023

*Document Version*  
Publisher's PDF, also known as Version of record

[Link back to DTU Orbit](#)

*Citation (APA):*  
Madiot, G., Albrechtsen, M., Stobbe, S., Sotomayor-Torres, C. M., & Arregui, G. (2023). Multimode optomechanics with a two-dimensional optomechanical crystal. *APL Photonics*, 8(11), Article 116107. <https://doi.org/10.1063/5.0170883>

---

### General rights







Copyright and moral rights for the publications made accessible in the public portal are retained by the authors and/or other copyright owners and it is a condition of accessing publications that users recognise and abide by the legal requirements associated with these rights.

- Users may download and print one copy of any publication from the public portal for the purpose of private study or research.
- You may not further distribute the material or use it for any profit-making activity or commercial gain
- You may freely distribute the URL identifying the publication in the public portal

If you believe that this document breaches copyright please contact us providing details, and we will remove access to the work immediately and investigate your claim.

RESEARCH ARTICLE | NOVEMBER 08 2023

## Multimode optomechanics with a two-dimensional optomechanical crystal

Guilhem Madiot ; Marcus Albrechtsen ; Søren Stobbe ; Clivia M. Sotomayor-Torres ; Guillermo Arregui  

 Check for updates

APL Photonics 8, 116107 (2023)

<https://doi.org/10.1063/5.0170883>




View Online




Export Citation

CrossMark



yttrium iron garnet   glassy carbon   beamsplitters   fused quartz   additive manufacturing  
zeolites   III-IV semiconductors   gallium lump   copper nanoparticles   organometallics  
nano ribbons   barium fluoride   europium phosphors   photonics   infrared dyes  
sapphire windows   Nd:YAG   epitaxial crystal growth   ultra high purity materials   transparent ceramics   CIGS  
spintronics   raman substrates   cerium oxide polishing powder   cermet   nanodispersions  
silver nanoparticles   perovskites   surface functionalized nanoparticles   Al   Si   P   S   Cl   Ar   MBE grade materials   thin film  
MOCVD   beta-barium borate   K   Ca   Sc   Ti   V   Cr   Mn   Fe   Co   Ni   Cu   Zn   Ga   Ge   As   Se   Br   Kr   OLED lighting   solar energy  
rare earth metals   quantum dots   Rb   Sr   Y   Zr   Nb   Mo   Tc   Ru   Rh   Pd   Ag   Cd   In   Sn   Sb   Te   I   Xe   sputtering targets   fiber optics  
osmium   scintillation Ce:YAG   Cs   Ba   La   Hf   Ta   W   Re   Os   Ir   Pt   Au   Hg   Tl   Pb   Bi   Po   At   Rn   h-BN   deposition slugs  
refractory metals   laser crystals   Fr   Ra   Ac   Th   Pa   U   Np   Pu   Am   Cm   Bk   Cf   Es   Fm   Md   No   Lr   CVD precursors   photovoltaics  
anodic aluminum oxide   niobate   InAs wafers   Ce   Pr   Nd   Pm   Sm   Eu   Gd   Tb   Dy   Ho   Er   Tm   Yb   Lu   metamaterials   borosilicate glass  
25th Anniversary logo   MOFs   AuNPs   Th   Pa   U   Np   Pu   Am   Cm   Bk   Cf   Es   Fm   Md   No   Lr   YBCO   superconductors   InGaAs  
ZnS   CdTe   The Next Generation of Material Science Catalogs   indium tin oxide   MgF2   rutile  
perovskite crystals   transparent ceramics   diamond micropowder   optical glass



Now Invent.™

www.americanelements.com  
© 2001-2022, American Elements LLC, a U.S. Registered Trademark



# Multimode optomechanics with a two-dimensional optomechanical crystal

Cite as: APL Photon. 8, 116107 (2023); doi: 10.1063/5.0170883

Submitted: 5 August 2023 • Accepted: 20 October 2023 •

Published Online: 8 November 2023



Guilhem Madiot,<sup>1</sup>  Marcus Albrechtsen,<sup>2</sup>  Søren Stobbe,<sup>2,3</sup>  Clivia M. Sotomayor-Torres,<sup>1,4</sup>   
and Guillermo Arraqui<sup>2,a)</sup> 

## AFFILIATIONS

<sup>1</sup>Catalan Institute of Nanoscience and Nanotechnology (ICN2), CSIC and BIST, Campus UAB, Bellaterra 08193, Barcelona, Spain

<sup>2</sup>Department of Electrical and Photonics Engineering, DTU Electro, Technical University of Denmark, Building 343, DK-2800 Kgs. Lyngby, Denmark

<sup>3</sup>NanoPhoton - Center for Nanophotonics, Technical University of Denmark, Ørstedes Plads 345A, DK-2800 Kgs. Lyngby, Denmark

<sup>4</sup>ICREA - Institució Catalana de Recerca i Estudis Avançats, 08010 Barcelona, Spain

<sup>a)</sup> Author to whom correspondence should be addressed: [guibra@dtu.dk](mailto:guibra@dtu.dk)

## ABSTRACT

Chip-scale multimode optomechanical systems have unique benefits for sensing, metrology, and quantum technologies relative to their single-mode counterparts. Slot-mode optomechanical crystals enable sideband resolution and large optomechanical couplings of a single optical cavity to two microwave-frequency mechanical modes. Still, previous implementations have been limited to nanobeam geometries, whose effective quantum cooperativity at ultralow temperatures is limited by their low thermal conductance. In this work, we design and experimentally demonstrate a two-dimensional mechanical–optical–mechanical (MOM) platform that dispersively couples a slow-light slot-guided photonic-crystal waveguide mode and two slow-sound  $\sim 7$  GHz phononic wire modes localized in physically distinct regions. We first demonstrate optomechanical interactions in long waveguide sections, unveiling acoustic group velocities below 800 m/s, and then move on to mode-gap adiabatic heterostructure cavities with a tailored mechanical frequency difference. Through optomechanical spectroscopy, we demonstrate optical quality factors  $Q \sim 10^5$ , vacuum optomechanical coupling rates,  $g_o/2\pi$ , of 1.5 MHz, and dynamical back-action effects beyond the single-mode picture. At a larger power and adequate laser-cavity detuning, we demonstrate regenerative optomechanical oscillations involving a single mechanical mode, extending to both mechanical modes through modulation of the input laser drive at their frequency difference. This work constitutes an important advance toward engineering MOM systems with nearly degenerate mechanical modes as part of hybrid multipartite quantum systems.

© 2023 Author(s). All article content, except where otherwise noted, is licensed under a Creative Commons Attribution (CC BY) license (<http://creativecommons.org/licenses/by/4.0/>). <https://doi.org/10.1063/5.0170883>

## I. INTRODUCTION

The study of the interaction between an electromagnetic resonator and a mechanical resonator in a cavity-optomechanical system has led to scientific and technological advances in quantum physics, nonlinear optics, and condensed matter physics.<sup>1–3</sup> However, the canonical theoretical description of the one-to-one interaction<sup>1</sup> fails to describe certain phenomena observed in realistic devices, which naturally host multiple optical and mechanical modes,<sup>4</sup> i.e., multimode optomechanical systems, which can cause quantum decoherence when the collective interaction is uncontrolled.<sup>5,6</sup> In the usual experimental setting with a single laser drive, undriven optical modes are usually unimportant. However,

the individual parametric optomechanical couplings of the various mechanical modes to the driven optical mode lead to an effective coupling between them. The case of two mechanical modes, i.e., mechanical–optical–mechanical (MOM) systems, has witnessed particular attention due to its potential impact in the quantum regime, e.g., to probe decoherence processes,<sup>7–9</sup> to introduce nonreciprocity,<sup>10</sup> or to enhance robustness to thermal noise via mode squeezing.<sup>11</sup> In addition, its linearized Hamiltonian description is particularly suited for the study of exceptional points,<sup>12–14</sup> while strongly driven MOM devices exhibit collective nonlinear dynamics, including mode competition,<sup>15,16</sup> synchronization,<sup>17,18</sup> and bistability control.<sup>19</sup> At the frontier between these two fields of study—namely the linear and nonlinear regimes—lies the so far

largely unexplored paradigm of nonlinear non-Hermitian physics, where phenomena such as topological mode transfer and unidirectional phonon emission could be realized based on high-frequency coherent phonon self-oscillations.<sup>20–22</sup>

The optically mediated coupling between mechanical modes in MOM systems scales inversely with their frequency difference and becomes symmetrical only when their respective vacuum optomechanical coupling rates to the common optical cavity mode,  $g_{o,1}$  and  $g_{o,2}$ , are identical. This has fostered research on physical implementations that exhibit (nearly) degenerate mechanical modes, where the modes coherently mix into optomechanically dark and bright dressed states<sup>23</sup> and can transfer energy efficiently.<sup>24</sup> These include Fabry–Pérot microcavities with two identical membranes,<sup>25</sup> membrane-in-the-middle cavities with symmetry-enforced (high-order) mechanical mode degeneracies,<sup>24</sup> or parallel evanescently coupled optical resonators. The latter category exploits the strong dependence of the frequencies of the resulting optical supermodes on the distance between the resonators and embraces double-disk microcavities,<sup>26</sup> bilayer photonic-crystal cavities,<sup>27</sup> and photonic-crystal zipper cavities.<sup>28</sup> Interestingly, the electromagnetic boundary conditions across material interfaces lead to a strong local field enhancement, i.e., a slot-mode effect, when such distances are deep sub-wavelength and the field polarization is adequate.<sup>29</sup> Such an effect is non-resonant; therefore, the formation of supermodes is not required. This has allowed integrated MOM devices with large optomechanical couplings by using triple nanobeam geometries separated by tenths of nanometers, each supporting one of the excitations.<sup>30</sup> These quasi-one-dimensional (1D) MOM slot-mode optomechanical crystals (OMCs) can display microwave-frequency phononic-crystal cavity modes and reach the sideband-resolved regime, which has recently allowed the observation of mechanical exceptional points.<sup>31</sup> However, their geometries may be unsuitable to study emergent macroscopic quantum phenomena in millikelvin MOM systems because of inefficient thermalization.<sup>32</sup> In the presence of residual absorption, the limited heat dissipation pathways of 1D OMCs lead to a phononic hot bath that can destroy the prepared quantum states. In addition, the poor stiffness of nanobeams makes them prone to surface-force-induced collapses during and after fabrication,<sup>33</sup> limiting how narrow the gap between them can be, i.e., how large  $g_o$  can be,<sup>30,34</sup> and potentially requiring stress-release management.<sup>30,35</sup>

Two-dimensional (2D) optomechanical structures can sustain even larger optical quality factors,<sup>36,37</sup> large  $g_o$  to long-lived hyper-sonic mechanical modes,<sup>32,38</sup> and have the additional benefits of enhanced heat dissipation<sup>32,39</sup> and convenient stiffness. Nonetheless, to the best of our knowledge, no experimental work has focused so far on MOM experiments in 2D OMCs. Here, we propose a novel waveguide and cavity optomechanics platform that enables the coupling of a slot-guided optical mode to two independent, nearly degenerate, microwave-frequency mechanical modes. By building mode-gap adiabatic heterostructure cavities,<sup>40</sup> we demonstrate a sideband-resolved system with  $g_o$  as high as 1.5 MHz between C-band telecom photons in a cavity with a  $Q \sim 10^5$  and two  $\sim 7$  GHz acoustic resonators. Passive control over the frequency difference of the latter two via a geometrical parameter is achieved, which may enable tailored MOM systems adaptable to specific experimental requirements. By performing wavelength and power-dependent optomechanical spectroscopy of a device with mechanical modes

only differing in frequency by 6 MHz, we provide evidence of multi-mode dynamical back-action in good agreement with the linearized optomechanical equations of motion of a MOM system. Finally, we demonstrate simultaneous self-oscillatory dynamics of two mechanical resonators stimulated by an intermodulation tone, consistent with recent demonstrations using two mechanical modes of a single nanobeam OMC cavities.<sup>41</sup>

## II. SLOT-MODE MULTIMODE OPTOMECHANICAL CRYSTAL WAVEGUIDES

The geometry of the multimode OMC waveguides (OMCWs) we explore here consists of a line defect waveguide composed of two rows of circular holes with (optionally) different radii  $R_1$  and  $R_2$ , a slot of width  $s$ , and two triangular lattices of shamrock-shaped<sup>42,43</sup> holes around them, with the shamrocks facing each other [Fig. 1(a)]. The waveguide axis ( $x$ ) is oriented along the silicon [110] crystalline direction. The structures are fabricated on a 220 nm silicon-on-insulator (SOI) platform, and the 2  $\mu\text{m}$  buried oxide is undercut to release the suspended structures with hydrofluoric vapour-phase etching. The patterns are defined in a chemically semi-amplified resist with electron-beam lithography<sup>29</sup> and etched into the silicon using dry-etching based on a modified CORE process.<sup>44,45</sup> The fabrication process is tailored to yield an excellent design-to-realized pattern fidelity, including smooth and vertical sidewalls [Fig. 1(a), insets].<sup>46</sup> The presence of the slot mechanically decouples the two membrane sides, making the system a MOM OMCW with a geometry-controlled mechanical frequency difference provided by  $\Delta R = R_1 - R_2$ . The employed shamrock crystal enables large near-infrared electromagnetic<sup>45</sup> and GHz mechanical bandgaps,<sup>47</sup> and a similar geometry has been exploited for the *in situ* generation of coherent acoustic phonons using Anderson-localized optical modes resulting from residual roughness in the etched sidewalls.<sup>45</sup> However, the quality factors,  $Q$ , observed in Ref. 45 were limited due to a multimode optical dispersion of the slot-guided mode and much below those measured in a slot photonic-crystal waveguide solely based on circular holes.<sup>48</sup> The geometry we propose leverages the best features of both shamrock-shaped and circular holes as it exhibits single-mode dispersions with zero group velocity, i.e., simultaneous slow light and sound, at the mechanical and optical Bloch wavevectors where forward-type intra-modal Brillouin interactions are phase-matched,<sup>49,50</sup> respectively, at  $q = 0$  and  $k = \pi/a_x$  [Fig. 1(b)]. In addition, the vector parities of the Bloch optical ( $y$ - and  $z$ -symmetric  $\mathbf{E}$  fields) and mechanical ( $z$ -symmetric) modes make them optomechanically bright. The electric field amplitude of the optical mode,  $|\mathbf{E}(\mathbf{r})|$ , the displacement amplitude,  $|\mathbf{u}(\mathbf{r})|$ , and the deformation profile of the mechanical mode of interest are shown in Fig. 1(b). The former exhibits subwavelength light confinement in the etched air slot, making the band edge frequency very sensitive to slot-width variations,<sup>29,30</sup> while the latter is reminiscent of the in-plane breathing mode of a nanobeam waveguide, where one of the lateral free boundary conditions is replaced by a full-gap phononic crystal.<sup>51</sup> The independent breathing motion of the two phononic waveguides [the mechanical mode is only represented for the bottom mechanical waveguide in Fig. 1(b)] strongly modulates the slot width, which leads to large unit-cell vacuum optomechanical coupling rates,  $g_{o,\text{cell}}/2\pi$ , of 4.8 MHz, between the optical and the two mechanical Bloch modes. Departure from mechanical-mode

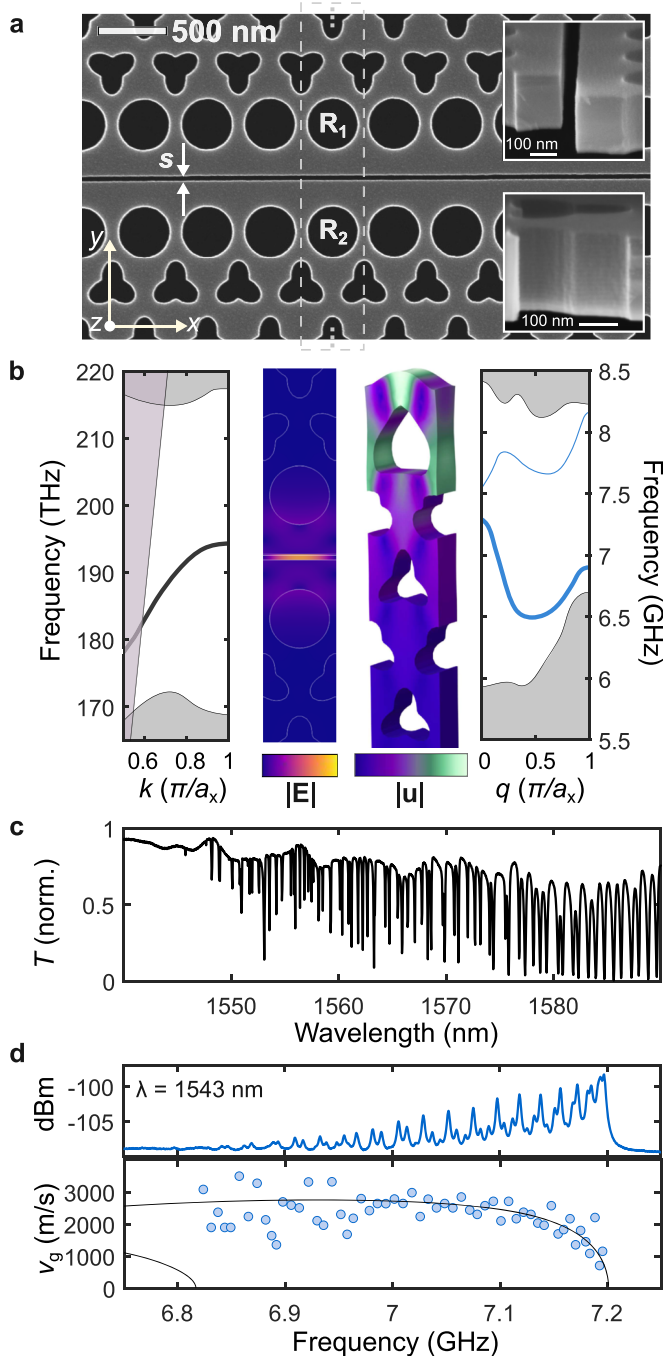


**FIG. 1.** Multimode optomechanical crystal waveguides (OMCWs). (a) Scanning electron micrograph of an OMCW that couples two phononic waveguide modes—one on each side of the air slot—to a slot-guided optical mode. Insets: cross section of the slot (top) and a cleaved shamrock. (b) Optical (left) and mechanical (right) dispersion diagrams of the structure in (a). The Bloch modes of interest are represented at  $k = \pi/a_x$  and  $q = 0$ . (c) Optical transmission spectrum of a mirror-terminated OMCW ( $L = 350a_x$ ) through a tapered fiber loop. (d) Radio frequency (RF) spectrum measured with a laser drive on an optical mode at  $\lambda = 1543$  nm, and comparison of the simulated (line) and experimentally reconstructed (blue circles) acoustic group velocity.

degeneracy when the radii difference is  $\Delta R \neq 0$  has a negligible effect on the respective values of  $g_{o,cell}/2\pi$  (see Sec. S1 of the supplementary material for more details about the band structures as a function of  $\Delta R$ ).

We probe the optical and mechanical properties of the OMCWs using a tunable diode laser connected to an optical fiber circuit that leads to a tapered fiber loop placed in contact with the slot waveguide. We terminate long OMCWs with short 32 unit cell waveguide segments within which the horizontal pitch is expanded from  $a_{x,1} = 484$  nm to  $a_{x,2} = 510$  nm. These sections behave simultaneously as optical and acoustic mirrors, forming standing waves in the central waveguide region<sup>45</sup> (see Sec. S1 of the supplementary material for dispersion diagrams as a function of  $a_x$ ). Sharp spectral dips in the transmitted optical signal [Fig. 1(c)] evidence evanescent coupling to resonant optical modes of the waveguide. We observe three spectral regions with distinct features: first, a region above  $\lambda \sim 1580$  nm made of Fabry–Pérot optical modes with a large on-resonance coupling fraction and a free spectral range (FSR) determined by the group index,  $n_g$ , and the length,  $L$ , of the waveguide; second, the wavelength region  $1560$  nm  $< \lambda < 1580$  nm, within which the coupling fraction is also large, but the resonant wavelengths are seemingly random. We attribute these resonances also to Fabry–Pérot modes whose wavelengths are perturbed by the presence and exact position of the loop (see Sec. III for a discussion of the dispersive effects of the loop on a single resonant optical mode). The third region is close to the band edge ( $\lambda > 1560$  nm) where strong slow-light-induced backscattering from sidewall roughness leads to Anderson-localized modes at random spectro-spatial locations, leading to a random FSR and strong mode-to-mode fluctuations in the coupling fraction.<sup>45,48</sup>

We characterize the mechanical properties of the OMCWs by moderate power and blue-detuned driving of optical modes in the first and second regions. We detect the thermal motion of the Fabry–Pérot standing mechanical modes using a fast photoreceiver and an electronic spectrum analyzer. A characteristic radio frequency (RF) spectrum for an Anderson-localized optical mode at  $\lambda = 1543$  nm is shown in Fig. 1(d). No degeneracy-lifting between the two independent phononic waveguide modes is observed for the case shown ( $\Delta R = 0$ ). The spectrum comprises multiple overlapping and regularly spaced Lorentzian-shaped mechanical resonances with estimated linewidths,  $\Gamma_m$ , in the range 2–5 MHz. In general, the coupling rate,  $g_o$ , between an Anderson-localized mode and the different acoustic Fabry–Pérot modes is hard to predict, notably because Anderson modes may display several spatial peaks at random distances.<sup>48</sup> In the case of Fig. 1(d), we employ the Anderson-localized mode with the shortest resonant wavelength, which appears to be tightly localized to a single spatial maximum. In that case, its  $k$ -space representation is centered around the wavevector of the waveguide at that frequency,<sup>52</sup> i.e., at  $k \sim \pi/a_{x,1}$ . This may explain the steady growth of the overall transduction amplitude envelope as the mechanical band edge at 7.2 GHz is approached as the result of a relaxed phase-matching condition between an optical mode at  $k = \pi/a_{x,1}$  and mechanical modes at and around  $q = 0$  for forward-type Brillouin scattering interactions in a finite waveguide.<sup>50</sup> While Fig. 1(d) only exhibits peaks within the single-mode regime, RF spectra obtained by driving other optical modes also reveal peaks in the multi-mode propagation regime, in which the FSR is ill-defined due to inter-modal mechanical mixing. Using five



additional RF spectra, we reconstruct the acoustic group velocity,  $v_g$ , of the top and bottom phononic waveguides for  $\Delta R = 0$  (see Sec. S3 of the supplementary material for additional spectra and details on the reconstruction of  $v_g$ ). The reconstructed  $v_g$  is shown at the bottom of Fig. 1(d) and compared with the simulated  $v_g$ . The simulation curve has rigidly been offset by only  $-90$  MHz ( $\sim 1\%$  of  $\Omega_m$ ) to

account for potential systematic errors on the SEM-extracted contour of the geometric features, illustrating good agreement between simulations and measurements. We measure slow propagation of  $\sim 7$  GHz acoustic waves down to a group velocity below 800 m/s, constituting a sevenfold reduction relative to the transverse speed of sound in bulk silicon.

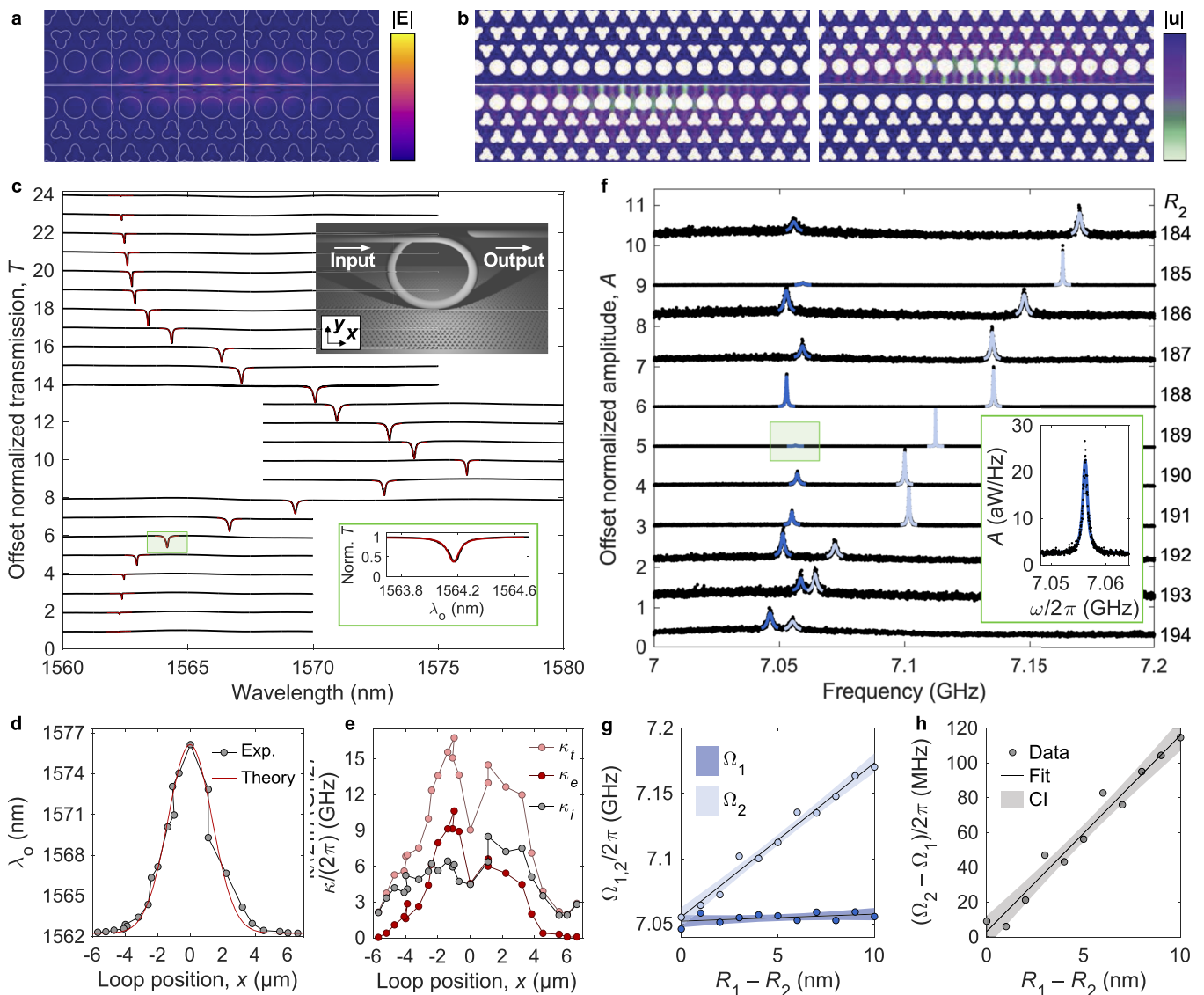


**FIG. 2.** Optomechanical spectroscopy of a 2D slot-mode mechanical–optical–mechanical (MOM) system. (a) Electric field amplitude,  $|E|$ , of the optical cavity mode and (b) displacement amplitude,  $|u|$ , and deformation profiles of the two mechanical cavity modes. (c) Normalized transmission spectrum at different positions along the waveguide axis,  $x$ . The spectra are offset for clarity, and the red curves are Lorentzian fits to the resonances. The insets show a schematic of the configuration with the loop on top of the cavity (top) and a close-up of a normalized spectrum (bottom). (d) Resonant wavelength as a function of the loop position, extracted from the fits in (a) and through a convolution of the calculated electric field intensity,  $|E|^2$ , with a Gaussian ( $\sigma = 0.99 \mu\text{m}$ ). (e) Total, external, and intrinsic decay rates as a function of the loop position. (f) Normalized radio frequency (RF) spectra measured for devices with a decreasing circular hole radius  $R_2$ . The spectra are offset for clarity. The blue solid lines are Lorentzian fits to the individual peaks. The inset shows a characteristic power spectral density of and fit to a single mechanical peak. (g) Extracted mechanical frequencies of the two plates (circles), linear fit (solid line), and confidence interval of the fit (shaded background). (h) Same as (e) for their frequency difference.

29 November 2023 12:13:09

### III. SLOT-MODE MULTIMODE OPTOMECHANICAL CRYSTAL CAVITIES

The efficient coupling of a multitude of Fabry-Pérot mechanical modes and Anderson-localized optical modes in the mirror-enclosed 2D OMCWs presented above provides an interesting platform to explore collective effects in multimode optomechanics, such as light squeezing.<sup>4</sup> However, some of the strongest optomechanical effects beyond the canonical one-to-one interaction occur in the MOM configuration. To explore such a setting, we engineer a MOM OMC cavity (OMCC) that couples two mechanical resonators and a high-Q optical mode based on the waveguide modes of Fig. 1 and the respective partial bandgaps above their band-edge frequencies. We adiabatically tune the horizontal pitch,  $a_x$ , along the waveguide axis from a central defect unit cell ( $a_{x,1} = 484$  nm) to mirror unit cells ( $a_{x,2} = 510$  nm) on both sides. The full defect region is formed by  $N_c = 15$  unit cells, and additional invariant sections made of  $N_m = 32$  mirror unit cells are included at the edges of the defect to prevent in-plane losses. Figure 2(a) shows the amplitude of the electric field,  $|E|$ , of the cavity mode for  $\Delta R = 0$ , whose theoretical resonant wavelength and quality factor are  $\lambda_o = 1556$  nm and  $Q_i = 1.05 \times 10^8$ . The deformation profile and displacement amplitude,  $|u|$ , of the two mechanical modes are shown in Fig. 2(b), and both have mechanical frequency  $\Omega_{1,2}/2\pi = 7.15$  GHz in the degenerate case. The frequency difference between the two mechanically decoupled mechanical cavity modes is controlled by decreasing  $R_2$  relative to  $R_1$ , which, in turn, slightly redshifts the resonant wavelength of the optical cavity mode. More details on the cavity-optomechanical figures of merit are provided in Sec. S2 of the supplementary material.

We characterize the optical and mechanical properties of the MOM OMCCs using the same fiber-loop evanescent technique as shown in Fig. 1. To account for the strong perturbative effect of the fiber loop on the resonant wavelength and losses of the optical cavity mode and infer their unperturbed parameters, i.e., in the absence of the loop, we systematically study the optical response as a function of the loop position. Figure 2(c) shows the optical transmission spectra across the cavity resonance for 24 different loop positions,  $x$ , with the loop in contact with the sample and approximately aligned to the slot axis [Fig. 2(c), top inset]. The position is extracted via the analysis of microscope images acquired with a  $100\times$  objective by imaging the probed structure from above. By moving the sample under the loop while in contact, the loop slides along the slot and changes its overlap with the optical cavity mode. We extract the resonant wavelength,  $\lambda_o$ , and the extrinsic,  $\kappa_e/2\pi$ , and intrinsic,  $\kappa_i/2\pi$ , decay rates of the cavity mode for each loop position by fitting the cavity resonance with a Lorentzian line shape [Fig. 2(c), bottom inset], and using that, the on-resonance transmission is given by  $T_0 = (1 - \kappa_e/\kappa_i)^2$ , with  $\kappa_t = \kappa_e + \kappa_i$ . Figure 2(d) shows the extracted  $\lambda_o$  along with a theoretical prediction obtained from a convolution between the calculated  $|E|^2$  and a Gaussian envelope representing the loop.<sup>29</sup> The Gaussian has a standard deviation,  $\sigma = 0.99$   $\mu\text{m}$ , identified with a least-mean-square optimization. When the loop is centered on top of the cavity, the dispersive perturbation is maximal, shifting the wavelength by as much as  $\sim 15$  nm, i.e., 1% of the cavity wavelength. We identify the center position,  $x = 0$ , as the position causing the largest redshift of the resonance wavelength. The evolution of the total, extrinsic, and intrinsic decay rates as a function of the loop position is shown

in Fig. 2(e). Several interesting properties can be observed. First,  $\kappa_i$  changes considerably with the loop position, which implies that the loop not only loads the cavity but also adds additional undetected loss pathways. Second, we observe a decrease in both  $\kappa_i$  and  $\kappa_e$  when the loop is centered on the cavity. We hypothesize that this is due to the additional symmetry of this configuration. Third, when the loop is far from the geometric cavity center ( $>4$   $\mu\text{m}$ ), we see that it no longer couples to the cavity (i.e.,  $\kappa_e$  vanishes) and the cavity wavelength converges to  $\lambda_o = 1562$  nm, which implies that this configuration may probe the unperturbed cavity. However, while an unperturbed wavelength can be extracted, it is unclear if  $\kappa_i$  has also converged, indicating that the employed technique may not fully allow the measurement of the unperturbed optical linewidth. Therefore, we conservatively estimate  $\kappa_i/2\pi < 2$  GHz (for the  $R_2 = 193$  nm here).

We systematically characterize the mechanical cavity modes for OMCCs with different values of  $R_2$  as shown in Fig. 1(d), with the fiber loop positioned to achieve a minimal perturbation and critical coupling to the optical cavity mode, i.e.,  $T_0 = 1/2$ . The value of  $R_2$  is nominally reduced in 1 nm steps from  $R_1 = R_2 = 194$  nm to  $R_2 = 184$  nm. Figure 2(f) shows the RF spectra with Lorentzian fits to both mechanical modes. Following the prediction of the finite-element simulations (see Secs. S1 and S2 of the supplementary material), we identify the lower (higher) frequency mechanical mode, fitted in dark (light) blue, as that of the top (bottom) membrane. This probably holds true except for the smaller values of  $\Delta R$ , where the effect of disorder-induced dispersion might overcome the as-designed deterministic frequency difference. We note that the relative amplitude of the transduced signals is determined by the exact loop position transverse to the slot axis, which determines to what extent the modes are dampened, and by the presence of dynamical back-action effects, which may occur preferentially for one of the modes at a fixed detuning.<sup>15</sup> Despite this, the signal-to-noise ratio (SNR) remains sufficient to extract the central frequencies accurately. Figure 2(g) shows the extracted frequencies as well as linear fits predicting  $\Omega_1(\Delta R)/2\pi = 7.052(2)$  GHz +  $0.5(4)\Delta R$  MHz/nm and  $\Omega_2(\Delta R)/2\pi = 7.055(3)$  GHz +  $11.8(5)\Delta R$  MHz/nm. The non-zero slope found for  $\Omega_1$  likely originates from short-range proximity effects,<sup>29,46</sup> i.e., the smaller value for  $R_2$  leads to a smaller effective electron-beam dose on the other membrane side, which is not accounted for with standard long-range proximity effect correction.<sup>47</sup> Meanwhile, the slope of  $\Omega_2$  agrees well with the simulation prediction [10.19(7) MHz/nm]. Note that the mechanical frequencies are  $\sim 90$  MHz lower than the simulated values, which is in very good agreement with the theory-experiment offset found for the acoustic waveguide band of Fig. 1(d). Figure 2(h) shows  $\delta\Omega(\Delta R)/2\pi$ , illustrating its linear dependence with an intercept  $\delta\Omega(0)/2\pi = (3 \pm 4)$  MHz. This non-zero intercept corroborates that we consistently observe a separation of a few MHz between the nominally degenerate mechanical modes, which is caused by inherent fabrication imperfections. The values of  $\kappa_i$  under the measurement conditions of Fig. 2(f) are all in reasonable agreement with those reported in Fig. 2(e), i.e., we observe no pronounced effect of  $\Delta R$  on the optical  $Q$  (as expected from simulations; see Fig. S3 of the supplementary material), and therefore, the MOM OMCCs we demonstrate are all in the sideband-resolved regime ( $\kappa_i < \Omega_{1,2}$ ). In addition, the values of  $g_{o,1}/2\pi$  and  $g_{o,2}/2\pi$  are measured to be

in the range of 1.2–1.5 MHz, which is in excellent agreement with simulations (see Secs. S2 and S4 of the supplementary material for details on the simulated and measured  $g_{o,1}$  and  $g_{o,2}$ ). In Sec. IV, we explore the implications of the reported cavity-optomechanical figures of merit and the MOM nature of the system on the detuning- and power-dependence of the dynamical back-action effects on a laser-driven device with nearly degenerate mechanical modes.

#### IV. OPTOMECHANICAL SPECTROSCOPY OF A MECHANICAL-OPTICAL-MECHANICAL SYSTEM

We consider a structure with  $R_1 = 194$  nm and  $R_2 = 193$  nm and place the loop in the position previously indicated, leading to loss rates of  $\kappa_i/2\pi \approx 3.5$  GHz and  $\kappa_e/2\pi \approx 0.76$  GHz and a resonance wavelength (at low power) of  $\lambda_0 = 1559.35$  nm. Using a laser power of  $P_{in} = 131 \mu\text{W}$ , we step-scan the laser wavelength,  $\lambda$ , from the blue-detuned side of the optical resonance and measure the RF spectrum. In Fig. 3(a), we show the resulting power spectral density as a colormap, highlighting the two mechanical resonances separated by  $\sim 6$  MHz. To track the mechanical frequencies and linewidths as a function of  $\lambda$ , we fit each spectrum with a sum of two

Lorentzians. Examples of the fitted spectra are presented in Fig. 3(b), with experimental data extracted from Fig. 3(a) as indicated by the white dashed lines. The same procedure is applied for  $P_{in} = 87, 131, 175,$  and  $219 \mu\text{W}$ , and the extracted parameters are summarized in Figs. 3(c)–3(e) (left column). For increasing input power, the mechanical resonances experience an increasing displacement around their natural value [Fig. 3(c)] due to optomechanical dynamical back-action. Meanwhile, the mechanical damping rates tend to decrease down to a minimum, as expected in the blue-detuned regime. For sufficiently high input power (here at  $P_{in} = 219 \mu\text{W}$ ), the damping rate saturates around  $\sim 10$  kHz, which indicates that the mode is self-oscillating.<sup>1</sup> In Figs. 3(c)–3(e) (right column), we qualitatively compare the extracted parameters as a function of laser wavelength with the values predicted by the linearized optomechanical equations of motion of a MOM system.<sup>13,53</sup> In addition to the optical parameters given above, the model uses  $\Omega_{1,2}/2\pi = 7.061 \text{ GHz} \pm 3.05 \text{ MHz}$ ,  $\Gamma_1/2\pi = \Gamma_2/2\pi = 3.2 \text{ MHz}$ ,  $g_{o,1}/2\pi = 1.25 \text{ MHz}$ , and  $g_{o,2}/2\pi = 1.5 \text{ MHz}$ . The details on the theoretical model are given in Sec. S6 of the supplementary material. We note that the model ignores the observed residual-absorption-mediated thermal non-linearities, so the horizontal axis in the theoretical plots of Figs. 3(c)–3(e), which use the laser detuning

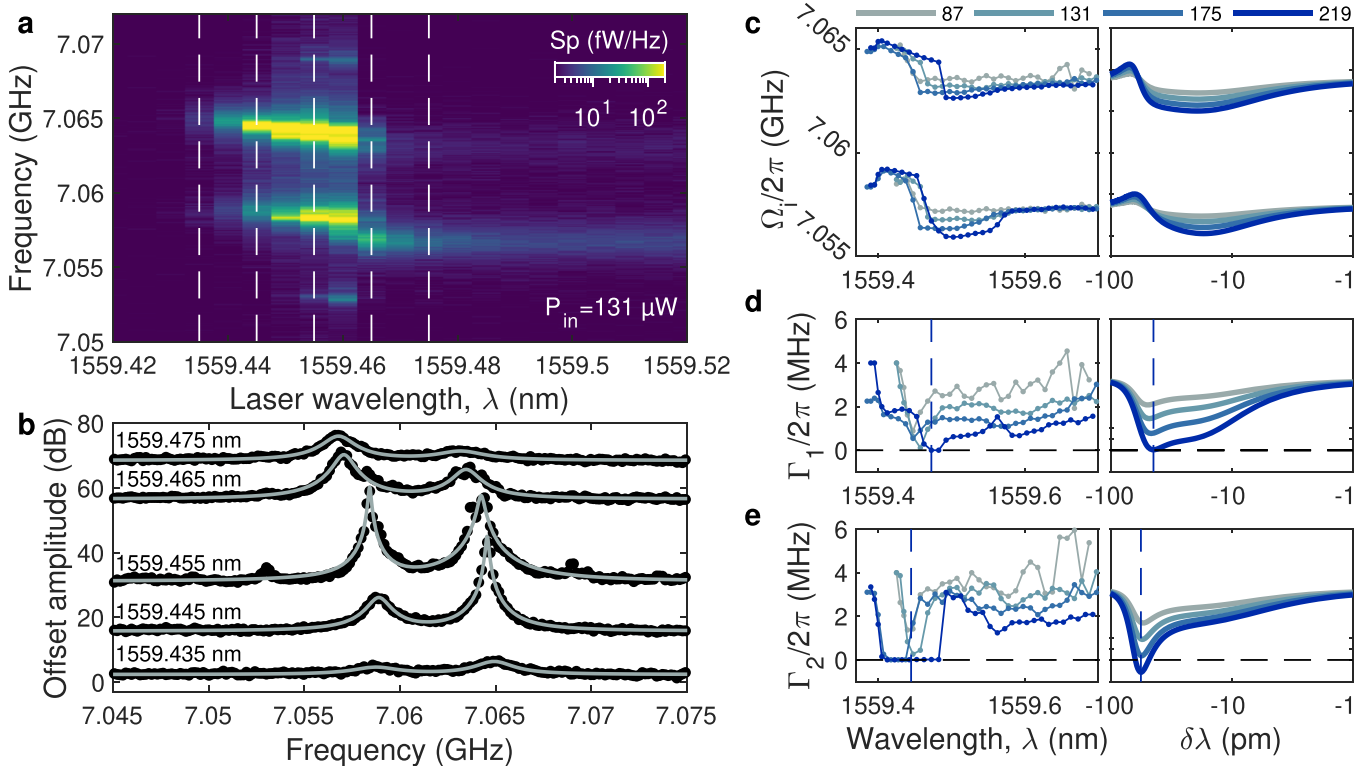


**FIG. 3.** Dynamical back-action in the nearly degenerate case. (a) Measured radiofrequency (RF) spectra as a function of the laser wavelength  $\lambda$  for a laser power  $P_{in} = 131 \mu\text{W}$ . The white dashed lines indicate the value of  $\lambda$  for the spectra in (b). (b) Individual RF spectra (black dots) fitted with a double-Lorentzian function (gray solid lines) to extract the mechanical frequencies and damping rates. The curves are vertically offset for clarity. (c)–(e) Experimental (left) and theoretical (right) evolution of (c) the mechanical frequencies  $\Omega_1$  and  $\Omega_2$ , and the mechanical damping rates (d)  $\Gamma_1$  and (e)  $\Gamma_2$ . These parameters are plotted at four different powers (see the legend with  $P_{in}$  indicated in units of  $\mu\text{W}$ ) and as a function of  $\lambda$  or the laser-cavity detuning,  $\delta\lambda$ , respectively, for experiment and theory. The blue lines indicate the wavelength (or detuning) at which the minimum of the damping rates occur for  $P_{in} = 219 \mu\text{W}$ .

29 November 2023 12:13:09



$\delta\lambda = \lambda - \lambda_0$ , cannot be directly mapped to the horizontal axis of the experimental plots as the true detuning scales non-linearly with the laser wavelength due to the thermo-optic drag, i.e.,  $\lambda_0 = f(\lambda)$ . Nevertheless, the latter produces a nearly asymptotic decrease in  $\delta\lambda$  toward zero (see Sec. S5 of the supplementary material), followed by a sudden jump in the red-detuned regime ( $\delta\lambda > 0$ ). Therefore, theory and experiment can be qualitatively compared by using a logarithmic scale for the horizontal axis of the theoretical plots. We observe that the model captures the overall evolution of the mechanical frequencies and damping rates. In particular, the damping rates reach their minimum at different values of  $\lambda$  (or  $\delta\lambda$ ), as highlighted with the dashed lines for the case  $P_{in} = 219 \mu\text{W}$ . This feature, which does not emerge in a model with two independent optomechanical oscillators (comparison shown in Sec. S5 of the supplementary material), suggests that the mechanical modes start hybridizing despite their non-identical mechanical frequencies. The same applies to any asymmetrical feature in the relative evolution of the parameters of both mechanical modes. We note that below  $\lambda \approx 1559.4 \text{ nm}$ , the SNR of the transduced mechanical resonances is very low, which prevents determining the frequencies and damping rates. Furthermore, above  $\lambda \approx 1559.7$ , the properties of the modes stabilize, and their transduction slowly decreases until the laser exits the thermo-optic resonance.

**V. STIMULATED TWO-MODE OPTOMECHANICAL AMPLIFICATION VIA INTERMODULATION**

The simultaneous parametric amplification of two thermally excited mechanical oscillators coupled to a common optical mode is typically prevented by mode competition,<sup>15</sup> leading to anomalous cooling,<sup>54</sup> except for the case of two mechanical resonators of disparate frequency.<sup>30,53</sup> Nevertheless, such two-mode amplification can be stimulated by modulating the input laser intensity at the inter-modal frequency.<sup>41</sup> To demonstrate such a feature in the investigated MOM OMCC, we focus on a device with  $R_1 = 194 \text{ nm}$  and  $R_2 = 190 \text{ nm}$ , which results in a frequency difference of  $\delta\Omega/2\pi \approx 38 \text{ MHz}$ . We fix the optical loading conditions as before, with a blue-detuned driving at a power  $P_{in} = 90 \mu\text{W}$  and considerably below the self-oscillation threshold. We then apply a direct intensity modulation of the laser with a modulation depth  $d$  and a frequency  $\Omega_{VNA}$ . We report in Fig. 4(a) the recorded RF spectrum for  $d = 30\%$  while step-scanning the modulation frequency. We observe the two mechanical modes at  $\Omega_1/2\pi = 6.965 \text{ GHz}$  and  $\Omega_2/2\pi = 7.003 \text{ GHz}$  with respective linewidths—when the modulation is off— $\Gamma_1/2\pi = 2.417 \text{ MHz}$  and  $\Gamma_2/2\pi = 1.234 \text{ MHz}$ . Note that the mechanical frequencies are slightly lower than those reported in Figs. 2(f)–2(h) because the device we analyze here used a lithography mask with exposed (void) features shrunk by 5 nm uniformly. Each mechanical peak is surrounded by a pair of sidebands at a distance of  $\pm\Omega_{VNA}$ . When the high-frequency (low-frequency) sideband of the peak at  $\Omega_1$  ( $\Omega_2$ ) crosses the mode at  $\Omega_2$  ( $\Omega_1$ ), i.e., when  $\Omega_{VNA} = \delta\Omega$ , the amplitude of the mechanical peaks increases significantly, far beyond (by at least 20 dB) the value given by the sum of the thermal transduction and the sideband peak. In Fig. 4(b), we show three spectra extracted from the upper map, corresponding to  $\Omega_{VNA} < \delta\Omega$ , in which case the two modes are thermally excited (bottom),  $\Omega_{VNA} \approx \delta\Omega$ , where the modes amplify by nearly 40 dB

(middle), and  $\Omega_{VNA} > \delta\Omega$ , for which the amplitudes of the modes reduce down to that of the sub-threshold regime (top).

In order to identify the dynamical range enabling stimulated multimode lasing to occur, we record the transduced amplitudes of both mechanical modes as a function of both modulation parameters  $d$  and  $\Omega_{VNA}$ . Figure 4(c) represents the SNR evaluated based on the mode amplitude in the absence of modulation, i.e., in its unaltered thermal regime. For each mode, we plot the lasing threshold calculated from the theory in Ref. 41 using  $g_{o,1}/2\pi = g_{o,2}/2\pi = 1.5 \text{ MHz}$ ,  $\lambda_0 = 1579.895 \text{ nm}$ ,  $\kappa_i = 2.074 \text{ GHz}$ , and  $\kappa_e = 0.664 \text{ GHz}$ . The theory is calculated using the optical detuning  $\Delta$  as a fitting parameter, since the presence of thermo-optic effect prevents its independent determination. However, we note that the asymmetry of the amplification area about  $\Omega_{VNA}$  is finely determined by the laser detuning  $\Delta$  and is symmetric when the optomechanical

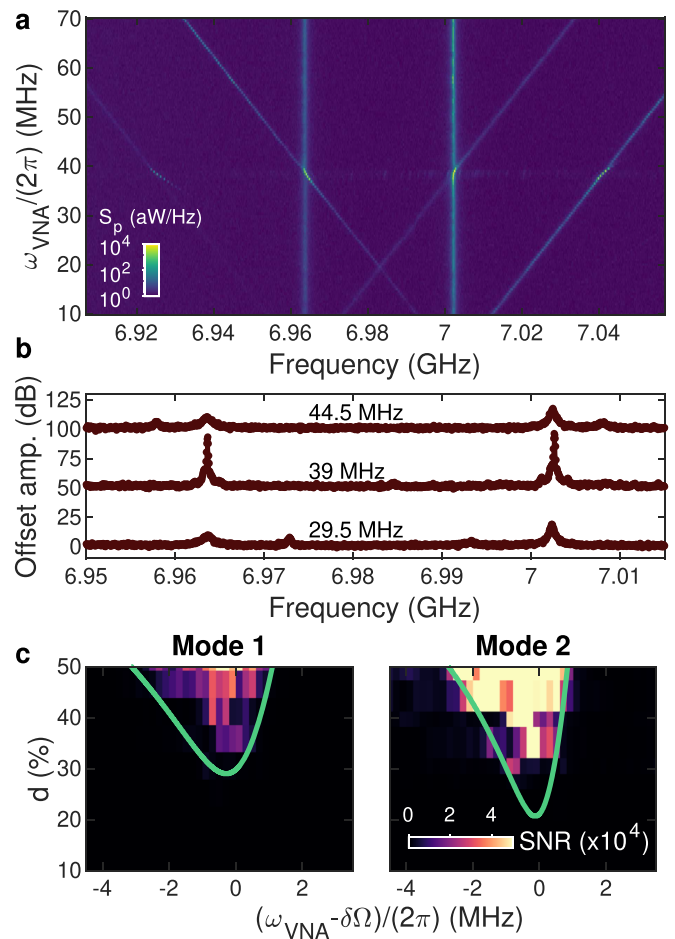


**FIG. 4.** Simultaneous Floquet mechanical lasing of two nearly degenerate mechanical modes. (a) Measured RF spectra as a function of the modulation frequency,  $\Omega_{VNA}$ . (b) Individual RF spectra extracted from (a) and vertically offset for clarity. (c) Measured RF peak amplitude as a function of the modulation depth and modulation frequency for mechanical modes 1 (left) and 2 (right). The green lines are the theoretical amplification threshold obtained using  $\Delta = 1.024\Omega$  (with  $\Omega = 6.984 \text{ GHz}$ ) and the model in Ref. 41.

29 November 2023 12:13:09

amplification is optimal, i.e., at  $\Delta = \bar{\Omega}$ , where  $\bar{\Omega} = 6.984$  GHz is the mean mechanical frequency. This allows for an unambiguous fit using  $\Delta = 1.024\bar{\Omega}$  and leads to a qualitative agreement of the theory with the experimental findings. Note that the second mechanical mode reaches the lasing threshold at a lower modulation depth because of its significantly lower damping rate ( $\Gamma_2 < \Gamma_1$ ).

## VI. CONCLUSION AND OUTLOOK

In summary, we have demonstrated a 2D OMC design that can operate as a sideband-resolved multimode MOM cavity-optomechanical system with two  $\sim 7$  GHz mechanical modes at a close spectral distance,  $\delta\Omega_{1,2} \ll \Omega_{1,2}$ , and a high- $Q$  optical cavity ( $Q \sim 10^5$ ). The measured optomechanical coupling rates reaching  $g_o/2\pi \sim 1.5$  MHz are among the largest values observed in OMCCs with microwave-frequency mechanical modes, enabling low-power self-oscillations of the individual mechanical modes and simultaneous lasing upon modulation of the laser drive at their frequency difference. The latter is shown to be controlled, starting from the nominally degenerate case, by slightly breaking a structural symmetry, which does not significantly degrade the aforementioned properties over the 120 MHz passive tuning range. By performing a wavelength and power-dependent spectroscopic analysis of a structure with nominally degenerate mechanical modes, we show that the features of multimode optomechanical back-action are observed. The combination of stochastic and deterministic deviations of the fabricated structure from the nominal design introduces a built-in frequency difference that we observe to be lower-bounded to around 4 MHz, preventing stronger optically induced hybridization, the exploration of exceptional points below the self-oscillation threshold, and the study of synchronization dynamics above it.<sup>55</sup> We foresee that introducing thermal tuning elements on both sides of the waveguide,<sup>56</sup> e.g., metallic bonding pads, will enable independent and low-crosstalk tuning of the mechanical frequencies, which will allow the proposed system to reach the degenerate case and explore the physics across the frequency-crossing. Given the investigated limitations imposed by the physical presence of the fiber loop on the optical and mechanical losses, we expect further improvement by incorporating butt-coupled<sup>32</sup> or side-coupled input/output waveguides.<sup>57</sup> Another necessary avenue required to leverage the improved heat dissipation of the 2D OMCs is the passivation, via termination chemistry<sup>58</sup> or encapsulation layers,<sup>59</sup> of the slot-sidewall defect states that leads to the thermo-optical bistability we observe and that generally prevents us from performing red-detuned optomechanical cooling. In addition, the prospects of self-assembling gaps way below the limits of top-down nanofabrication<sup>60</sup> may allow reaching  $g_o$  rates about four times larger than the ones we have already reported. Finally, the strong transduction of Fabry-Pérot mechanical modes we observe on the mirror-terminated waveguides and the demonstrated slow-down of sound to  $\sim 700$  m/s find application in injection-locked optomechanical oscillators,<sup>61</sup> on-chip phonon networks for information processing,<sup>51</sup> or phononic quantum memories.<sup>62</sup> Conversely, the sensitivity of slow sound to fabrication imperfection<sup>63</sup> and large ensemble measurements on mirror-terminated waveguides may allow for the observation of spectral features resulting from Anderson localization of hypersonic acoustic waves.<sup>64</sup>

## SUPPLEMENTARY MATERIAL

See the supplementary material for additional information on the waveguide and cavity finite-element simulations, the waveguide acoustic group velocity reconstruction, the experimental extraction of the optomechanical coupling rates, the correlation between laser wavelength and laser-cavity detuning in the presence of thermo-optic non-linearities, the theoretical modeling of a laser-driven MOM system, and the methodology used in the stimulated multimode lasing experiment.

## ACKNOWLEDGMENTS

The authors thank Karl Pelka for useful discussion. G.M. and C.M.S.-T. acknowledge the support from the project LEIT funded by the European Research Council, H2020 (Grant Agreement No. 885689). ICN2 is supported by the Severo Ochoa program from the Spanish Research Agency (AEI, Grant No. SEV-2017-0706) and by the CERCA Programme/Generalitat de Catalunya. M.A. and S.S. gratefully acknowledge funding from the Villum Foundation Young Investigator Program (Grant No. 13170). S.S. additionally acknowledges funding from the Danish National Research Foundation (Grant No. DNRF147—NanoPhoton), the Innovation Fund Denmark (Grant No. 0175-00022—NEXUS), the Independent Research Fund Denmark (Grant No. 0135-00315—VAFL), and the European Research Council (Grant No. 101045396—SPOTLIGHT). G.A. acknowledges the financial support from the European Union's Horizon 2021 research and innovation program under the Marie Skłodowska-Curie Actions (Grant No. 101067606—TOPEX).

## AUTHOR DECLARATIONS

### Conflict of Interest

The authors have no conflicts to disclose.

### Author Contributions

**Guilhem Madiot:** Conceptualization (equal); Data curation (equal); Formal analysis (equal); Investigation (equal); Methodology (equal); Project administration (equal); Resources (equal); Software (equal); Supervision (equal); Validation (equal); Visualization (equal); Writing – original draft (equal); Writing – review & editing (equal). **Marcus Albrechtsen:** Data curation (equal); Formal analysis (equal); Investigation (equal); Methodology (equal); Resources (equal); Validation (equal); Visualization (equal); Writing – original draft (equal); Writing – review & editing (equal). **Søren Stobbe:** Funding acquisition (equal); Project administration (equal); Resources (equal); Supervision (equal); Validation (equal); Writing – review & editing (equal). **Clivia M. Sotomayor-Torres:** Funding acquisition (equal); Project administration (equal); Resources (equal); Supervision (equal); Validation (equal); Writing – review & editing (equal). **Guillermo Arregui:** Conceptualization (equal); Data curation (equal); Formal analysis (equal); Funding acquisition (equal); Investigation (equal); Methodology (equal); Project administration (equal); Resources (equal); Software (equal); Supervision (equal); Validation (equal); Visualization (equal); Writing – original draft (equal); Writing – review & editing (equal).

## DATA AVAILABILITY

The data that support the findings of this study are available from the corresponding author upon reasonable request.

## REFERENCES

- <sup>1</sup>M. Aspelmeyer, T. J. Kippenberg, and F. Marquardt, *Rev. Mod. Phys.* **86**, 1391 (2014).
- <sup>2</sup>B.-B. Li, L. Ou, Y. Lei, and Y.-C. Liu, *Nanophotonics* **10**, 2799 (2021).
- <sup>3</sup>P. Meystre, *Ann. Phys.* **525**, 215 (2013).
- <sup>4</sup>W. H. P. Nielsen, Y. Tsaturyan, C. B. Möller, E. S. Polzik, and A. Schliesser, *Proc. Natl. Acad. Sci. U. S. A.* **114**, 62 (2017).
- <sup>5</sup>K. Børkje, A. Nunnenkamp, B. M. Zwickl, C. Yang, J. G. E. Harris, and S. M. Girvin, *Phys. Rev. A* **82**, 013818 (2010).
- <sup>6</sup>C. M. Pluchar, A. R. Agrawal, and D. J. Wilson, [arXiv:2307.03309](https://arxiv.org/abs/2307.03309) (2023).
- <sup>7</sup>H. Seok, L. F. Buchmann, E. M. Wright, and P. Meystre, *Phys. Rev. A* **88**, 063850 (2013).
- <sup>8</sup>M. J. Weaver, D. Newsom, F. Luna, W. Löffler, and D. Bouwmeester, *Phys. Rev. A* **97**, 063832 (2018).
- <sup>9</sup>G. Li, W. Nie, X. Li, M. Li, A. Chen, and Y. Lan, *Sci. China: Phys., Mech. Astron.* **62**, 100311 (2019).
- <sup>10</sup>L. Mercier de Lépinay, C. F. Ockeloen-Korppi, D. Malz, and M. A. Sillanpää, *Phys. Rev. Lett.* **125**, 023603 (2020).
- <sup>11</sup>J. Huang, D.-G. Lai, and J.-Q. Liao, *Phys. Rev. A* **108**, 013516 (2023).
- <sup>12</sup>A. Xuereb, C. Genes, and A. Dantan, *Phys. Rev. Lett.* **109**, 223601 (2012).
- <sup>13</sup>H. Xu, D. Mason, L. Jiang, and J. Harris, *Nature* **537**, 80 (2016).
- <sup>14</sup>P. Djorwe, Y. Pennec, and B. Djafari-Rouhani, *Phys. Rev. Appl.* **12**, 024002 (2019).
- <sup>15</sup>X. Zhang, T. Lin, F. Tian, H. Du, Y. Zou, F. S. Chau, and G. Zhou, *Appl. Phys. Lett.* **112**, 153502 (2018).
- <sup>16</sup>P. Djorwe, Y. Pennec, and B. Djafari-Rouhani, *Phys. Rev. E* **98**, 032201 (2018).
- <sup>17</sup>F. Bemani, A. Motazedifard, R. Roknizadeh, M. H. Naderi, and D. Vitali, *Phys. Rev. A* **96**, 023805 (2017).
- <sup>18</sup>J. Sheng, X. Wei, C. Yang, and H. Wu, *Phys. Rev. Lett.* **124**, 053604 (2020).
- <sup>19</sup>K. Pelka, G. Madiot, R. Braive, and A. Xuereb, *Phys. Rev. Lett.* **129**, 123603 (2022).
- <sup>20</sup>M. Benzaouia, A. D. Stone, and S. G. Johnson, *APL Photonics* **7**, 121303 (2022).
- <sup>21</sup>K. Ji, Q. Zhong, L. Ge, G. Beaudoin, I. Sagnes, F. Raineri, R. El-Ganainy, and A. M. Yacomotti, [arXiv:2212.06488](https://arxiv.org/abs/2212.06488) (2022).
- <sup>22</sup>A. Fischer, T. Raziman, W. K. Ng, J. Clarysse, J. Dranczewski, D. Saxena, S. Vezzoli, H. Schmid, K. Moselund, and R. Sapienza, [arXiv:2306.16112](https://arxiv.org/abs/2306.16112) (2023).
- <sup>23</sup>Q. Lin, J. Rosenberg, D. Chang, R. Camacho, M. Eichenfield, K. J. Vahala, and O. Painter, *Nat. Photonics* **4**, 236 (2010).
- <sup>24</sup>A. B. Shkarin, N. E. Flowers-Jacobs, S. W. Hoch, A. D. Kashkanova, C. Deutsch, J. Reichel, and J. G. E. Harris, *Phys. Rev. Lett.* **112**, 013602 (2014).
- <sup>25</sup>C. Gärtner, J. P. Moura, W. Haaxman, R. A. Norte, and S. Gröblacher, *Nano Lett.* **18**, 7171 (2018).
- <sup>26</sup>Q. Lin, J. Rosenberg, X. Jiang, K. J. Vahala, and O. Painter, *Phys. Rev. Lett.* **103**, 103601 (2009).
- <sup>27</sup>Y.-G. Roh, T. Tanabe, A. Shinya, H. Taniyama, E. Kuramochi, S. Matsuo, T. Sato, and M. Notomi, *Phys. Rev. B* **81**, 121101 (2010).
- <sup>28</sup>M. Eichenfield, R. Camacho, J. Chan, K. J. Vahala, and O. Painter, *Nature* **459**, 550 (2009).
- <sup>29</sup>M. Albrechtsen, B. Vosoughi Lahijani, R. E. Christiansen, V. T. H. Nguyen, L. N. Casse, S. E. Hansen, N. Stenger, O. Sigmund, H. Jansen, J. Mørk, and S. Stobbe, *Nat. Commun.* **13**, 6281 (2022).
- <sup>30</sup>K. E. Grutter, M. I. Davanço, and K. Srinivasan, *Optica* **2**, 994 (2015).
- <sup>31</sup>N. Wu, K. Cui, Q. Xu, X. Feng, F. Liu, W. Zhang, and Y. Huang, *Sci. Adv.* **9**, eabp8892 (2023).
- <sup>32</sup>H. Ren, M. H. Matheny, G. S. MacCabe, J. Luo, H. Pfeifer, M. Mirhosseini, and O. Painter, *Nat. Commun.* **11**, 3373 (2020).
- <sup>33</sup>E. Buks and M. L. Roukes, *Phys. Rev. B* **63**, 033402 (2001).
- <sup>34</sup>L. Midolo, A. Schliesser, and A. Fiore, *Nat. Nanotechnol.* **13**, 11 (2018).
- <sup>35</sup>R. M. Camacho, J. Chan, M. Eichenfield, and O. Painter, *Opt. Express* **17**, 15726 (2009).
- <sup>36</sup>A. H. Safavi-Naeini, T. P. M. Alegre, M. Winger, and O. Painter, *Appl. Phys. Lett.* **97**, 181106 (2010).
- <sup>37</sup>M. Winger, T. D. Blasius, T. P. Mayer Alegre, A. H. Safavi-Naeini, S. Meenehan, J. Cohen, S. Stobbe, and O. Painter, *Opt. Express* **19**, 24905 (2011).
- <sup>38</sup>C. M. Kersul, R. Benevides, F. Moraes, G. H. M. de Aguiar, A. Wallucks, S. Gröblacher, G. S. Wiederhecker, and T. P. Mayer Alegre, *APL Photonics* **8**, 056112 (2023).
- <sup>39</sup>L.-D. Haret, T. Tanabe, E. Kuramochi, and M. Notomi, *Opt. Express* **17**, 21108 (2009).
- <sup>40</sup>B.-S. Song, S. Noda, T. Asano, and Y. Akahane, *Nat. Mater.* **4**, 207 (2005).
- <sup>41</sup>L. Mercadé, K. Pelka, R. Burgwal, A. Xuereb, A. Martínez, and E. Verhagen, *Phys. Rev. Lett.* **127**, 073601 (2021).
- <sup>42</sup>I. Söllner, L. Midolo, and P. Lodahl, *Phys. Rev. Lett.* **116**, 234301 (2016).
- <sup>43</sup>G. Arregui, D. Navarro-Urrios, N. Kehagias, C. M. S. Torres, and P. D. García, *Phys. Rev. B* **98**, 180202 (2018).
- <sup>44</sup>V. T. H. Nguyen, C. Silvestre, P. Shi, R. Cork, F. Jensen, J. Hubner, K. Ma, P. Leussink, M. de Boer, and H. Jansen, *ECS J. Solid State Sci. Technol.* **9**, 024002 (2020).
- <sup>45</sup>G. Madiot, R. C. Ng, G. Arregui, O. Florez, M. Albrechtsen, S. Stobbe, P. D. García, and C. M. Sotomayor-Torres, *Phys. Rev. Lett.* **130**, 106903 (2023).
- <sup>46</sup>M. Albrechtsen, “Exploring novel physics and applications with high-resolution silicon nanofabrication,” Ph.D. thesis, Technical University of Denmark, 2023.
- <sup>47</sup>O. Florez, G. Arregui, M. Albrechtsen, R. C. Ng, J. Gomis-Bresco, S. Stobbe, C. M. Sotomayor-Torres, and P. D. García, *Nat. Nanotechnol.* **17**, 947 (2022).
- <sup>48</sup>G. Arregui, R. C. Ng, M. Albrechtsen, S. Stobbe, C. M. Sotomayor-Torres, and P. D. García, *Phys. Rev. Lett.* **130**, 043802 (2023).
- <sup>49</sup>A. H. Safavi-Naeini and O. Painter, *Opt. Express* **18**, 14926 (2010).
- <sup>50</sup>J. Kolvik, P. Burger, J. Frey, and R. Van Laer, *Optica* **10**, 913 (2023).
- <sup>51</sup>R. N. Patel, Z. Wang, W. Jiang, C. J. Sarabalis, J. T. Hill, and A. H. Safavi-Naeini, *Phys. Rev. Lett.* **121**, 040501 (2018).
- <sup>52</sup>V. Savona, *Phys. Rev. B* **83**, 085301 (2011).
- <sup>53</sup>R. C. Ng, P. Nizet, D. Navarro-Urrios, G. Arregui, M. Albrechtsen, P. D. García, S. Stobbe, C. M. Sotomayor-Torres, and G. Madiot, *Phys. Rev. Research* **5**, L032028 (2023).
- <sup>54</sup>U. Kemiktarak, M. Durand, M. Metcalfe, and J. Lawall, *Phys. Rev. Lett.* **113**, 030802 (2014).
- <sup>55</sup>M. Zhang, G. S. Wiederhecker, S. Manipatruni, A. Barnard, P. McEuen, and M. Lipson, *Phys. Rev. Lett.* **109**, 233906 (2012).
- <sup>56</sup>R. Burgwal and E. Verhagen, *Nat. Commun.* **14**, 1526 (2023).
- <sup>57</sup>S. Sonar, U. Hatipoglu, H. Ren, S. Meesala, D. Lake, and O. Painter, in *Conference on Lasers and Electro-Optics* (Optica Publishing Group, 2022), p. STh5F.2.
- <sup>58</sup>M. Borselli, T. J. Johnson, and O. Painter, *Appl. Phys. Lett.* **88**, 131114 (2006).
- <sup>59</sup>M. Borselli, T. J. Johnson, C. P. Michael, M. D. Henry, and O. Painter, *Appl. Phys. Lett.* **91**, 131117 (2007).
- <sup>60</sup>A. N. Babar, T. Weis, K. Tsoukalas, S. Kadkhodazadeh, G. Arregui, B. Vosoughi Lahijani, and S. Stobbe, [arXiv:2307.03309](https://arxiv.org/abs/2307.03309) (2023).
- <sup>61</sup>G. Modica, R. Zhu, R. Horvath, G. Beaudoin, I. Sagnes, and R. Braive, *Appl. Phys. Lett.* **117**, 193501 (2020).
- <sup>62</sup>A. Wallucks, I. Marinković, B. Hensen, R. Stockill, and S. Gröblacher, *Nat. Phys.* **16**, 772 (2020).
- <sup>63</sup>P. D. García, R. Bericat-Vadell, G. Arregui, D. Navarro-Urrios, M. Colombano, F. Alzina, and C. M. Sotomayor-Torres, *Phys. Rev. B* **95**, 115129 (2017).
- <sup>64</sup>G. Arregui, N. D. Lanzillotti-Kimura, C. M. Sotomayor-Torres, and P. D. García, *Phys. Rev. Lett.* **122**, 043903 (2019).